

Microstructure characterization and strengthening mechanisms of oxide dispersion strengthened (ODS) Fe-9%Cr and Fe-14%Cr extruded bars

Chauhan, A.; Bergner, F.; Etienne, A.; Aktaa, J.; de Carlan, Y.; Heintze, C.; Litvinov, D.; Hernandez-Mayoral, M.; Oñorbe, E.; Radiguet, B.; Ulbricht, A.;

Originally published:

August 2017

Journal of Nuclear Materials 495(2017), 6-19

DOI: <https://doi.org/10.1016/j.jnucmat.2017.07.060>

Perma-Link to Publication Repository of HZDR:

<https://www.hzdr.de/publications/Publ-25949>

Release of the secondary publication
on the basis of the German Copyright Law § 38 Section 4.

CC BY-NC-ND

Microstructure characterization and strengthening mechanisms of oxide dispersion strengthened (ODS) Fe-9%Cr and Fe-14%Cr extruded bars

A. Chauhan^{a*}, F. Bergner^b, A. Etienne^c, J. Aktaa^a, Y. de Carlan^d, C. Heintze^b, D. Litvinov^a, M. Hernandez-Mayoral^e, E. Oñorbe^e, B. Radiguet^c, A. Ulbricht^b

^aInstitute for Applied Materials, Karlsruhe Institute of Technology, Hermann-von-Helmholtz-Platz 1, 76344 Eggenstein Leopoldshafen, Germany

^bInstitute of Resource Ecology, Helmholtz-Zentrum Dresden - Rossendorf, Dresden 01328, Germany

^cGroupe de Physique des Matériaux, Université et INSA de Rouen, UMR CNRS 6634, Normandie Université, 76000 Rouen, France

^dDEN-Service de Recherches Métallurgiques Appliquées, CEA, Université Paris-Saclay, F-91191, Gif-sur-Yvette, France

^eMaterials of Energy Interest Division, Technology Department, CIEMAT, Avda. Complutense 40, 28040, Madrid, Spain

*email: ankur.chauhan@kit.edu , ankurskchauhan@gmail.com

Highlights

- Microstructure details derived from TEM, EBSD, SANS and APT are critically compared.
- Reported equations fed with microstructure parameters are applied to evaluate individual strengthening mechanisms.
- Along with the ODS alloys an extended set of alloys is considered to cover wide variations of microstructure.
- Linear summation of grain strengthening with Pythagorean summation of dislocation and particle strengthening describes the measured yield stress well.

Abstract

The collaborative study is focused on the relationship between microstructure and yield stress for an ODS Fe-9%Cr-based transformable alloy and an ODS Fe-14%Cr-based ferritic alloy. The contributions to the total room temperature yield stress arising from various strengthening mechanisms are addressed on the basis of a

comprehensive description of the microstructures uncovered by means of transmission electron microscopy (TEM), electron backscatter diffraction (EBSD), small-angle neutron scattering (SANS) and atom probe tomography (APT). While these methods provide a high degree of complementarity, a reasonable agreement was found in cases of overlap of information. The derived set of microstructure parameters along with reported strengthening equations was used to calculate the room temperature yield stress. The estimates were critically compared with the measured yield stress for an extended set of alloys including data reported for Fe-Cr model alloys and steels thus covering one order of magnitude or more in grain size, dislocation density, particle density and yield stress. The comparison shows that particle strengthening, dislocation forest strengthening, and Hall-Petch strengthening are the major contributions and that a mixed superposition rule reproduces the measured yield stress within experimental scatter for the whole extended set of alloys. The wide variation of microstructures additionally underpins the conclusions and goes beyond previous work, in which one or few ODS steels and narrow microstructure variations were typically covered.

Keywords: ODS steel; Strengthening mechanisms; TEM; APT; SANS

1. Introduction

Two sub-classes of advanced oxide-dispersion strengthened (ODS) Cr steels, also referred to as nanostructured steels, can be distinguished: ferritic Cr steels containing approximately 12 mass% or more Cr and transformable ferritic/martensitic (F/M) Cr steels containing less than 12 mass% Cr. Beyond current niche applications [1] and a wide spectrum of potential future non-nuclear and nuclear applications [2,3], this class of materials is considered to provide candidates for future Generation IV fission and fusion energy components. Indeed, feasibility via powder metallurgy route of ODS Fe-9%Cr, Fe-14%Cr and Fe-18%Cr tubes for sodium fast reactor fuel pin cladding was demonstrated [4,5].

These steels exhibit remarkable tensile strength, creep strength and excellent irradiation damage tolerance in comparison with other conventional heat resistant steels and austenitic steels due to the presence of uniformly dispersed nano-sized oxide particles. The advantages of nanoparticles are as follows: (1) they act as barriers for dislocation motion and grain boundary migration, which controls high-

temperature tensile properties and creep resistance [6–8]; and (2) they provide effective sinks for irradiation-induced defects, such as vacancies and interstitials, and nucleation sites for helium bubbles to suppress bubble formation, which ultimately offers high irradiation resistance [3,9,10]. These advantages in principle would allow for a higher operating temperature, which improves reactor's thermal efficiency.

Nevertheless, even though the nanoparticles significantly improve high temperature strength, it is reckoned to be achieved at the expense of ductility and toughness. For structural applications, such properties are of pivotal importance. Hence, it becomes critically vital to manipulate the contributions from various strengthening sources in order to optimize the combination of strength, ductility, toughness and other mechanical properties. Thus, identification of such strengthening sources and estimation of their respective contribution are of utmost importance. Furthermore, this insight can be further used as a basis for the evaluation of irradiation-induced hardness changes.

In this respect, few attempts have been made in past to clarify the strengthening mechanisms in ODS steels by taking all relevant strengthening contributors into consideration, and to provide reasonable models to calculate the yield stress in comparison with the experimental results [11–18]. It is well understood that the resistance of obstacles to dislocation glide determines the flow stress of alloys. The complex microstructure of ODS steels offers excellent strength due to the favorable superposition of several important strengthening mechanisms such as friction stress, solid solution strengthening, grain size strengthening, dislocation strengthening and oxide dispersion strengthening. However, in literature, different authors reported distinct strengthening mechanisms as most significant. Schneibel et al. [11], for PM2000 (ODS Fe20%Cr) and 14YWT (ODS Fe14%Cr), reported that Hall-Petch/grain size strengthening is comparable or even greater than the nano-particles strengthening. Kim et al. [14], for 14YWT, concluded grain boundary strengthening to be most significant. On the contrary, others, for 14YWT and ODS Fe12%Cr, confirmed dislocation forest strengthening as the main contributor [12,17].

As part of the European 7th framework program project MatISSE [19,20], two ODS alloys, a Fe-9%Cr-based transformable alloy and a Fe-14%Cr-based ferritic alloy, both in the product forms of extruded bars and tubes, were distributed among

partners in order to undergo a comprehensive and coordinated microstructural and mechanical examination. In particular, the micro- and nanostructure of the as-received materials was investigated using electron backscatter diffraction (EBSD), atom probe tomography (APT), small-angle neutron scattering (SANS) and transmission electron microscopy (TEM). These techniques are characterized by well-known specific strengths and limitations (e.g. resolution limits). Moreover, in combination they exhibit a number of complementarities and overlaps. It is therefore useful to pool results obtained from the application of individual techniques, check for consistency and derive a complete over-all picture. In the present effort, completeness means the ability to evaluate the dominant strengthening mechanisms based on simple strengthening expressions and to derive a meaningful estimation of the yield stress.

The objectives of the present work are:

- (1) To critically evaluate the characteristics of micro- and nano-structural features derived from different techniques;
- (2) To estimate the contributions from different strengthening mechanisms and to identify the dominant ones;
- (3) To reach and check a consistent description of strengthening for ODS and non-ODS steels/model alloys;
- (4) To set up a basis for the evaluation of irradiation-induced strength changes in ongoing work.

The materials and micro-/nanostructure characterization techniques are introduced in the experimental section. The results obtained for the ODS Fe9Cr and ODS Fe14Cr alloys are compiled and evaluated in section 3 to select a qualified microstructure data set used for the consideration of strengthening mechanisms. In order to additionally underpin the conclusions, a number of suitable alloys, for which data sets are reported in the literature, are added to the study. The discussion is aimed at evaluating the reliability of the uncovered micro-/nanostructure from the viewpoints of both the combination of techniques and the accuracy of the yield stress calculation. Moreover, the dominant strengthening mechanisms and the most probable type of superposition are worked out.

2. Experiments

2.1. Materials

The above mentioned yttria strengthened steels were developed and produced under the supervision of Commissariat à l'Énergie Atomique et aux Énergies Alternatives (CEA), France. Firstly, the pre-alloyed powders were produced by Aubert & Duval, France, by gas atomization. Mechanical alloying of the pre-alloyed powders with Y_2O_3 particles was performed at Plansee, Austria, under hydrogen atmosphere within a vertical attritor ball mill. The milled powders were then sealed in soft steel cans, followed by degassing and subsequently hot extruded into bars at 1100°C. Thereafter, the ODS Fe14Cr steel bar was annealed at 1150°C for 1.5 h and later distributed among partners for agreed investigations. The ODS Fe9Cr steel bar in ferritic (F) state was also distributed among partners who themselves performed required heat treatments (Table 1), depending upon specimen sizes, in order to mimic the tempered martensitic (TM) microstructure of tube material. The chemical compositions of the studied steels are shown in Table 2.

Table 1: Heat treatments performed on ODS Fe9Cr steel for specific techniques.

Heat treatment	1	2
Sample size	Cylindrical (d = 20.5 mm; l = 60 mm)	Cylindrical (d = 4.2 mm; l = 30 mm)
Heat treatments:		
1. Austenizing	At 1050 °C for 30 min	At 1050 °C for 10 min
2. Quenching	In oil at cooling rate of >20 K/s in the core of the sample	With He gas at cooling rate of 6–7 K/s
3. Tempering	At 750 °C for 1 h and air cooling	At 750 °C for 20 min and air cooling
Techniques	SANS	TEM/ EBSD/ Mechanical testing

Table 2: Chemical composition (in mass %) of the investigated ODS steels.

Material	Cr	W	Ti	Si	Mn	Ni	C	Y_2O_3	Fe
ODS Fe9Cr	9.1	1.1	0.3	0.3	0.3	0.2	0.1	0.25	Balance
ODS Fe14Cr	13.5	0.9	0.4	0.32	0.27	0.17	-	0.22	Balance

2.2. Methods

2.2.1. Microstructural characterization

Different versions of electron microscopy including TEM and EBSD were applied in the contributing labs for the purpose of specifying the type of microstructure (ferritic

versus martensitic), the degree of anisotropy/texture and grain size. The TEM studies were performed at Karlsruhe Institute of Technology (KIT), Germany, with a FEI TECNAI-20F microscope, at Centro de Investigaciones Energéticas, Medioambientales y Tecnológicas (CIEMAT), Madrid, Spain, and at CEA, France, with a JEOL JEM-2010 microscope; all operating at 200 keV. The EBSD patterns were acquired at KIT with a Zeiss EVO MA 10 scanning electron microscope (SEM) and at Helmholtz-Zentrum Dresden-Rossendorf (HZDR), Germany, with a Zeiss NVision 40 cross beam SEM both equipped with a Bruker e-Flash detector and analyzed with the QUANTAX ESPRIT software. Whereas, at CIEMAT a Hitachi SU6600 field emission gun (FEG) SEM equipped with an Oxford Instruments HKL NordlysF detector was used to obtain the EBSD patterns. The grain size distributions were measured with grain boundaries defined by a misorientation angle higher or equal to 5°. The meaning of the data will be specified in the results section.

SANS experiments were performed at the Instrument V4 at Helmholtz-Zentrum Berlin (HZB) [21] using a neutron wavelength of 0.605 nm. The samples of dimensions 9 x 9 x 1 or 10 x 10 x 1 (mm) were placed in a saturation magnetic field of 1.57 Tesla. In order to cover a sufficiently wide range of the scattering vector Q, two sample-detector distances of 1.7 m and 8 m were adjusted. The software package BerSANS [22] was used for corrections, absolute calibration, data reduction and separation of magnetic and nuclear scattering contributions. The transformation from scattering curves into particle-size distributions was performed using a Monte Carlo (MC) code [23] developed on the basis of an algorithm proposed by Martelli et al. [24].

APT analysis was performed at Groupe de Physique des Matériaux (GPM) in Université de Rouen Normandie, France, using a Cameca LEAP 4000X HR. Samples for APT were prepared in 2 steps, using standard electro polishing methods (1st step in 90% acetic acid plus 10% perchloric acid, 2nd step in 2% perchloric acid and 98% ethylenglycol). Experiments were conducted with electric pulses (pulse fraction equal to 20%, pulse repetition rate equal to 200 kHz) and a specimen temperature between 40 and 50K. 3D reconstruction was done with the IVAS 3.6.10 software. The reconstruction parameters were adjusted to get the good interplanar distances. The detailed analyses of the reconstructed volumes were performed with the GPM3D software v.6.1. Y and Ti oxides were identified using the isoposition method (IPM) developed by Da Costa [25]. This method is based on concentration

criteria. The ions used to set the concentration threshold were Y^{3+} , YO^{2+} , TiO^{2+} , CrO^{2+} and O^+ . As it was shown in [26], the APT analysis of nano-particles in ODS steels is subjected to strong bias. To correct this bias, Fe and Cr were removed from particle compositions and the size reported is the longest axis of the particles and not the Guinier radius.

2.2.2. Mechanical characterization

Tensile tests on ODS Fe9Cr steel were performed using an Instron 4505 universal testing machine equipped with an extensometer. Regarding ODS Fe14Cr steel, the tests were performed on a servo hydraulic MTS testing machine. Owing to the material quantity limitations, small tensile test specimens were used. With respect to ODS Fe9Cr steel, specimens with a gauge length of 13 mm and a gauge diameter of 2 mm were used. In the case of ODS Fe14Cr steel, specimens with a dog-bone geometry and a gauge section of $15 \times 3 \times 2$ mm were used. All specimens were machined parallel to the extrusion direction. For ODS Fe9Cr steel, tests were carried out with a nominal strain rate of 10^{-3} s^{-1} and for ODS Fe14Cr steel, a strain rate of 10^{-4} s^{-1} was chosen.

3. Results

3.1. TEM investigations

TEM bright field micrographs of ODS Fe9Cr extruded bar in both as-received as well as heat-treated conditions are shown in Fig.1. In as-received state (Fig.1a), the steel exhibits equiaxed grains with a dislocation density $(0.46 \pm 0.1) \times 10^{14} \text{ m}^{-2}$. The dark contrast Cr carbides are present both at grain boundaries and within the grains.

Upon heat treatment (Fig.1b), the steel manifests tempered martensitic structure with laths and subgrains having high dislocation density $(3.4 \pm 1.0) \times 10^{14} \text{ m}^{-2}$. The typical laths were several μm in length and $(0.25 \pm 0.01) \mu\text{m}$ in width. Additionally, irregular shaped Cr-W enriched carbides and Ti-enriched particles are distributed at various boundaries. For more details see Ref. [8].

In both states, complex Y–Ti–O nanoparticles are inhomogeneously distributed within the matrix. Nevertheless, regions with homogeneous particle distribution were also observed, for example see Fig. 2a. The density of the nanoparticles has been

estimated using such micrographs, where the nano-oxides density was homogeneous. They are listed in Table 3 and 4. From these TEM investigations, it can be concluded that the heat treatment did not change the size and distribution of the nanoparticles. High resolution TEM (HRTEM) investigations reveal face centered cubic $\text{Y}_2\text{Ti}_2\text{O}_7$ crystal structure for the examined particles. One such particle lattice (encircled) along with its corresponding fast Fourier transformation (FFT) power spectrum diffraction pattern from heat-treated ODS Fe9Cr steel is shown in Fig. 2b.

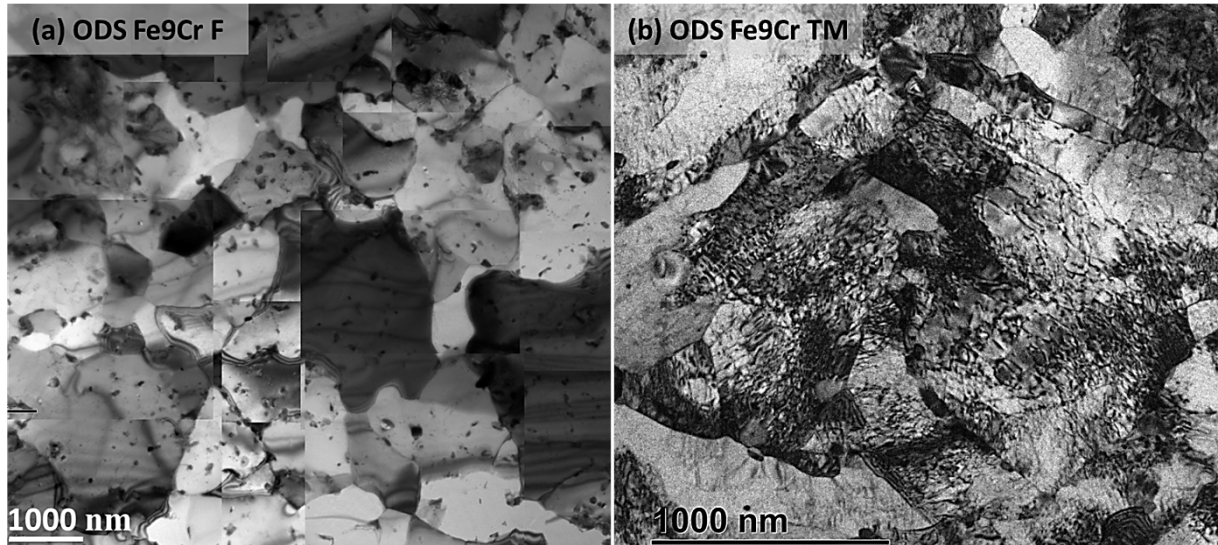


Fig. 1: TEM bright field micrographs revealing ODS Fe9Cr steel in (a) as-received state (ferritic) having dark contrast Cr carbides with low dislocation density (the collage was formed using 16 separate micrographs) and (b) heat-treated state (quenched and tempered) having tempered martensitic structure with high dislocation density.

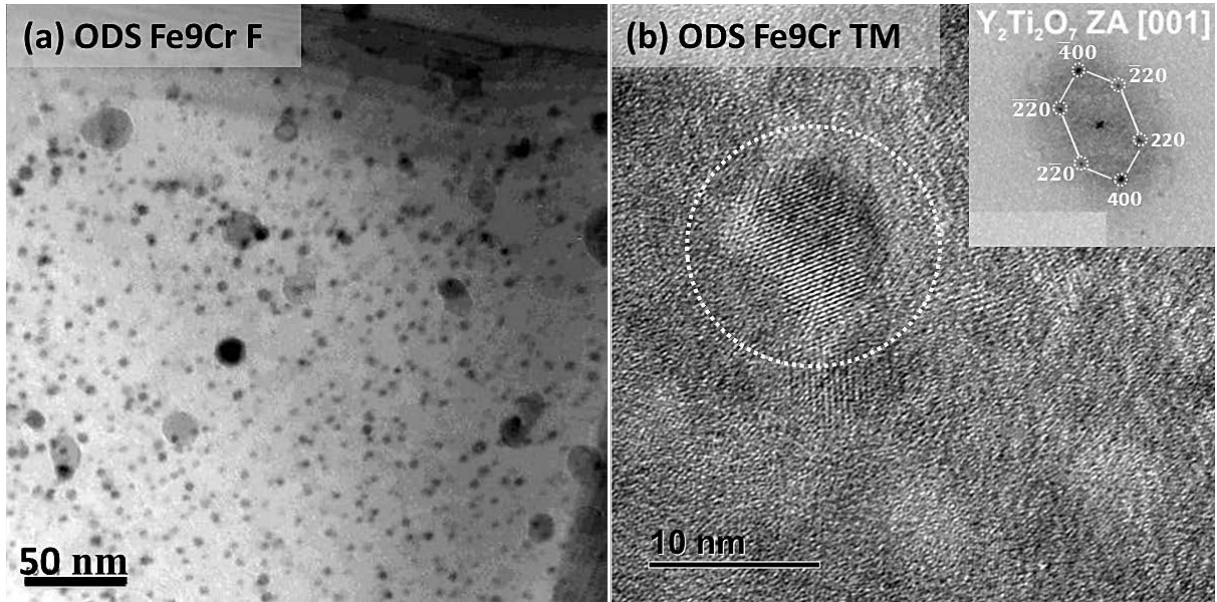


Fig. 2: (a) TEM bright filed micrograph from as-received ODS Fe9Cr steel revealing region with homogenous particle distribution. (b) High resolution TEM micrograph from heat-treated ODS Fe9Cr steel shows an $\text{Y}_2\text{Ti}_2\text{O}_7$ particle lattice (encircled) with [001] zone axis having face centered cubic crystal structure and its corresponding fast Fourier transformation (FFT) power spectrum diffraction pattern in inset.

TEM bright field micrographs from as-received ODS Fe14Cr extruded bar are shown in Fig. 3. In longitudinal direction (Fig. 3a), the grain structure appears to be composed of large elongated grains, together with regions of small equiaxed grains. In transverse direction (Fig. 3b), the grains are smaller and they do not exhibit elongated shape. Regarding dislocation structure, regions with different dislocation density are present. The average dislocation density is estimated to be about $5 \times 10^{14} \text{ m}^{-2}$. The observed strengthening nanoparticles are inhomogeneously distributed and they can be found forming lines, sometimes parallel to grain boundaries, as well as channels free of particles. The size distribution of particles can be classified in two ranges, smaller than 20 nm and larger than 20 nm, with regions where one or the other predominates (Fig. 4). The mean particle size and their number density are summarized in Table 5. The nanoparticles also show different morphologies, square or round, different composition and stoichiometry, implying different crystallography and interfacial structure. Careful examination of these particles, as reported separately (see Ref. [27]), reveals some of them enriched with Cr, Ti, Y, and W which decorate grain boundaries. Nevertheless, majority is of the Y-Ti-O nanoparticles which are observed within the grains along with the Al-rich and Ti-rich particles. For more details on TEM studies, we refer to Refs. [27,28].

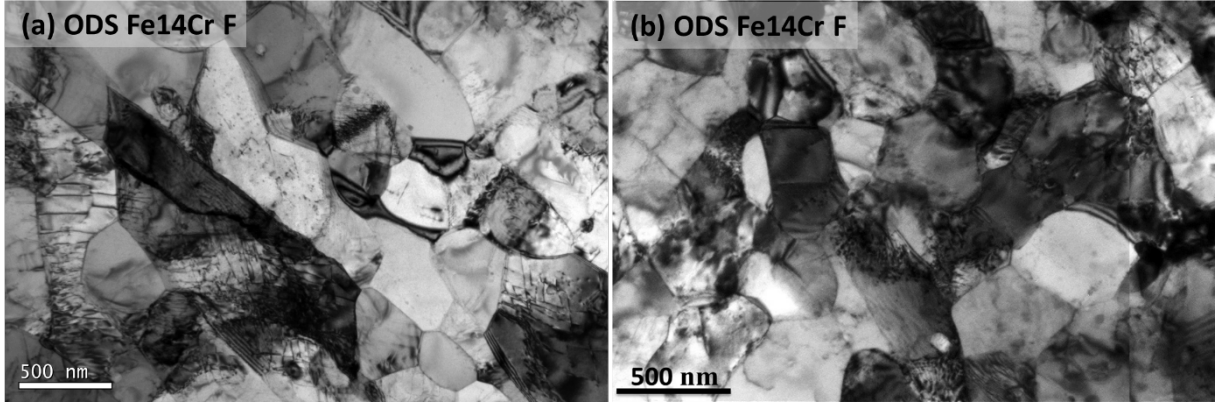


Fig. 3: TEM bright field micrographs from as-received ODS Fe14Cr steel (ferritic). (a) Longitudinal direction revealing elongated as well as equiaxed grains. (b) Transverse direction revealing small equiaxed grains. In both directions, regions with different dislocation density are apparent.

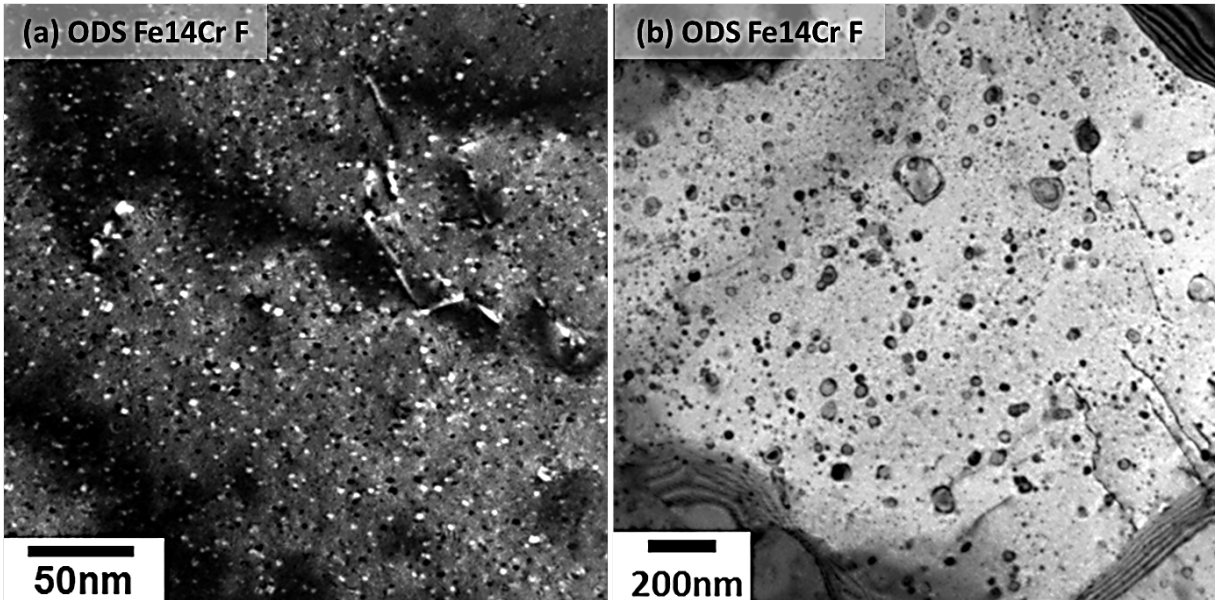


Fig. 4: TEM micrographs revealing nanoparticles distribution in ODS Fe14Cr steel. (a) Dark field shows particles smaller than 20 nm and (b) bright field unveils particles larger than 20 nm [27].

3.2. EBSD investigations

Typical inverse pole figure (IPF) maps obtained by EBSD for the as-received as well as heat-treated ODS Fe9Cr steel are shown in Fig. 5. The dissimilar colors of the grains in the IPF maps reveal the large difference in the orientation of the neighbor grains. Moreover, no texture was identified in the stereographic projections (not shown here). In both states, high- and low-angle grain boundaries are present. The misorientation analysis revealed that the fractions of high-angle grain boundaries (HAGB, $>15^\circ$) and low-angle grain boundaries (LAGB, $2-15^\circ$) in as-received state are

97% and 3%, respectively; whereas, in heat-treated state are 78% and 22%, respectively. The average grain sizes measured via EBSD for as-received and heat-treated states are $(1.19 \pm 0.03) \mu\text{m}$ and $(0.46 \pm 0.02) \mu\text{m}$, respectively.

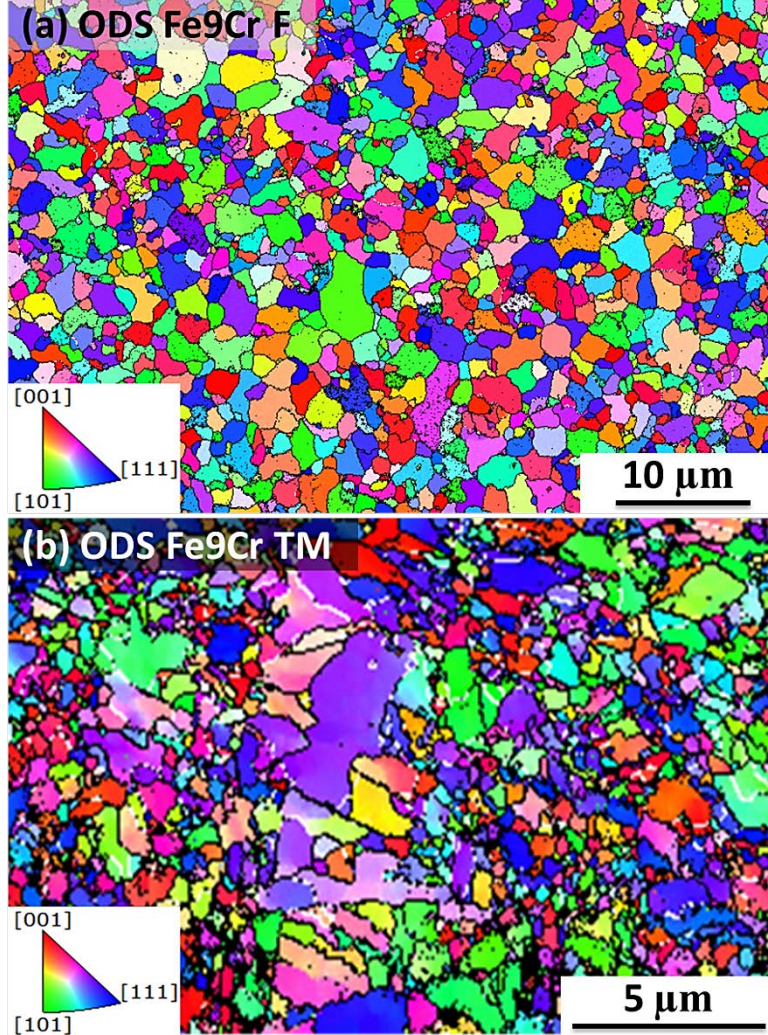


Fig. 5: Inverse pole figure maps obtained via EBSD for (a) as-received (step size: 72 nm) and (b) heat-treated (step size: 68 nm) ODS Fe9Cr steel (color keys for the crystallographic orientation are also shown); high-angle grain boundaries (HAGB, $>15^\circ$) are marked by black lines while low-angle grain boundaries (LAGB, 2 – 15°) are marked by white lines.

EBSD studies on as-received ODS Fe14Cr steel have been reported several times, see Refs. [27–29]. Briefly, the steel in longitudinal direction manifests bimodal grain size distribution, in which the smallest grains have distribution ranging from 0.1 to 3.0 μm , representing a volume fraction of 80%, whereas the largest and more elongated grains have sizes between 3.0 and 9.0 μm with a volume fraction of 20%. On the contrary, in the transverse plane, a more uniform distribution of grain size is observed, with a mean grain size of $(0.46 \pm 0.04) \mu\text{m}$. With respect to the texture, a preferential crystallographic orientation of the grains along $\langle 110 \rangle$ parallel to the

extrusion direction is observed (for example see Fig. 6). The misorientation analysis revealed that the fractions of HAGB and LAGB are 89% and 11%, respectively. The mean grain sizes obtained by EBSD are included in Tables 3 to 5.

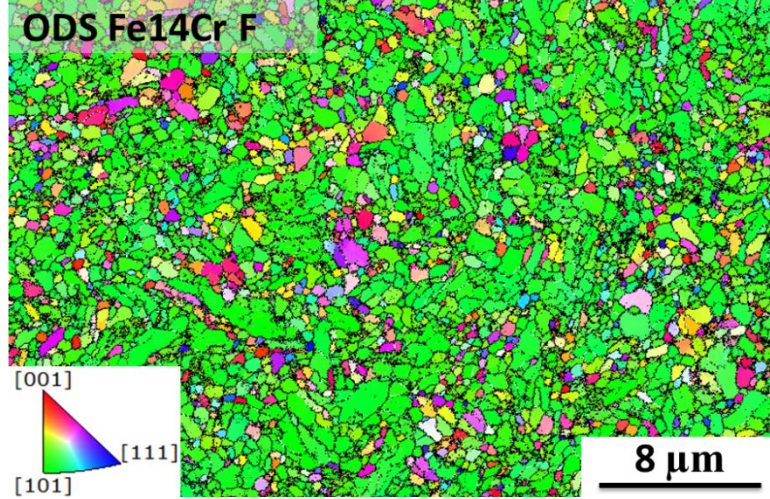


Fig. 6: Inverse pole figure map obtained via EBSD for as-received ODS Fe14Cr steel (step size: 48 nm) in transverse direction (color key for the crystallographic orientation is also shown).

3.3. SANS results

The measured magnetic scattering curves for ODS Fe9Cr extruded bar in the as-received and heat-treated conditions are plotted in Fig. 7a. The scattering curves for both conditions were found to agree in the Q-range from 0.3 to 3 nm⁻¹, which governs the size distribution of ODS particles. It can be concluded that the austenitization and subsequent quenching did not change the size distribution of scatterers. The MC fit of the difference between cross sections measured for the as-received condition and the background consisting of an adjusted part proportional to Q^4 and a constant incoherent scattering part derived from the Porod plot is shown in Fig. 7b.

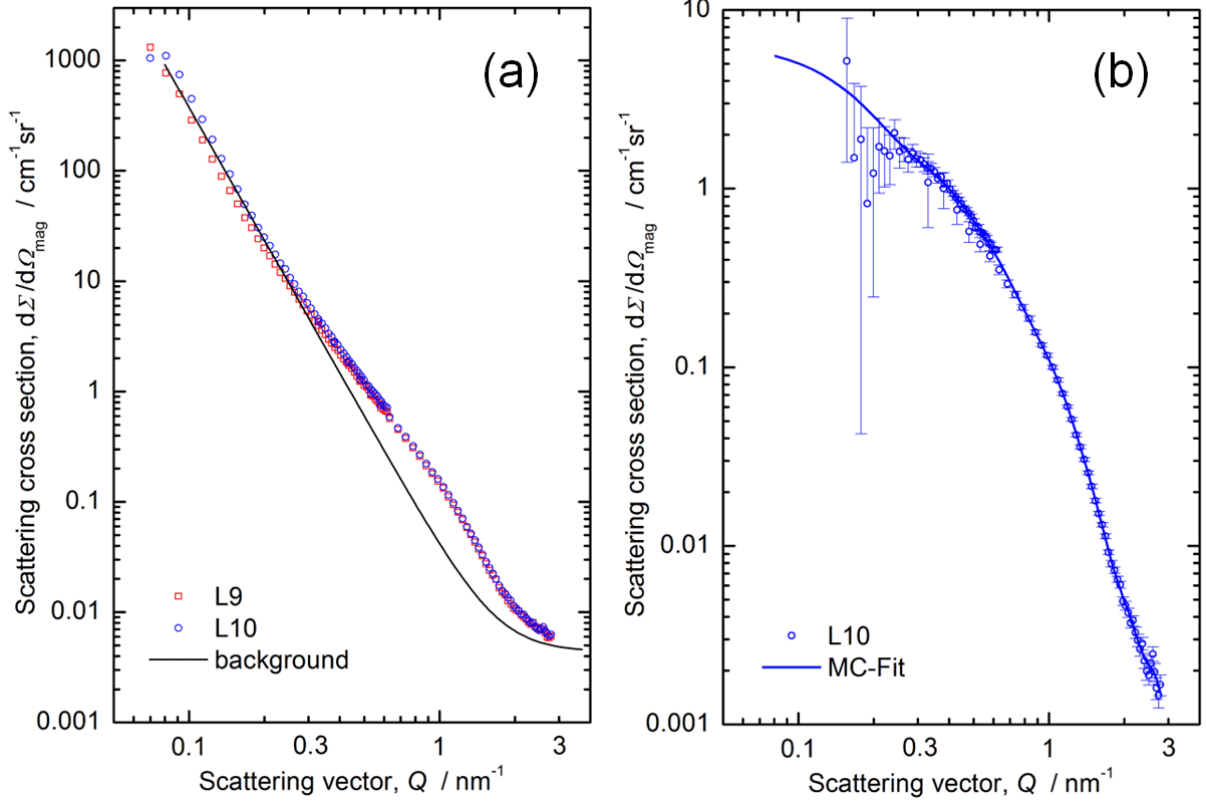


Fig. 7: (a) Scattering curves measured for the as-received condition (L10) and the heat-treated condition (L9) of ODS Fe9Cr and background consisting of an adjusted part proportional to Q^{-4} and constant incoherent scattering derived from the Porod plot, (b) measured difference scattering curve for the as-received condition (L10) and MC fit (see section 2.2).

The size distribution of oxide nanoparticles corresponding to the MC fit of the difference scattering curve for the as-received condition of ODS Fe9Cr extruded bar is shown in Fig. 8a. Scaling in absolute units was achieved by assuming non-magnetic scatterers dispersed in the ferromagnetic matrix. The size distribution for the ODS Fe14Cr extruded bar (sample L12) plotted in Fig. 8b was obtained according to the same procedure. The error ranges resulting from the MC fit are indicated as colored bands. It is interesting to note that the number density of nanoparticles in a yttria-free 14Cr reference (sample L11) is almost as high as the number density of nanoparticles in the ODS sample. This may be attributed to the formation of Cr-enriched oxide particles in the yttria-free sample due to the powder metallurgy fabrication steps under uncontrolled (or not perfectly controlled) oxygen partial pressures. The average A-ratios, $A = 1 + M/N$, where M and N are the magnetic and nuclear scattering contributions, respectively, are (2.5 ± 0.2) for ODS Fe9Cr, (2.3 ± 0.1) for yttria-free Fe14Cr and (3.25 ± 0.2) for ODS Fe14Cr. This indicates differences or similarities in the nanoparticle composition. For ODS Fe9Cr,

the A-ratio is consistent with $\text{Y}_2\text{Ti}_2\text{O}_7$ - and Y_2TiO_5 -type particles [30]. For Fe14Cr, the A-ratio does not give a straightforward indication on the type of nanoparticles. The resulting average characteristics of the nanoparticle size distributions are listed in Table 3 to 5.

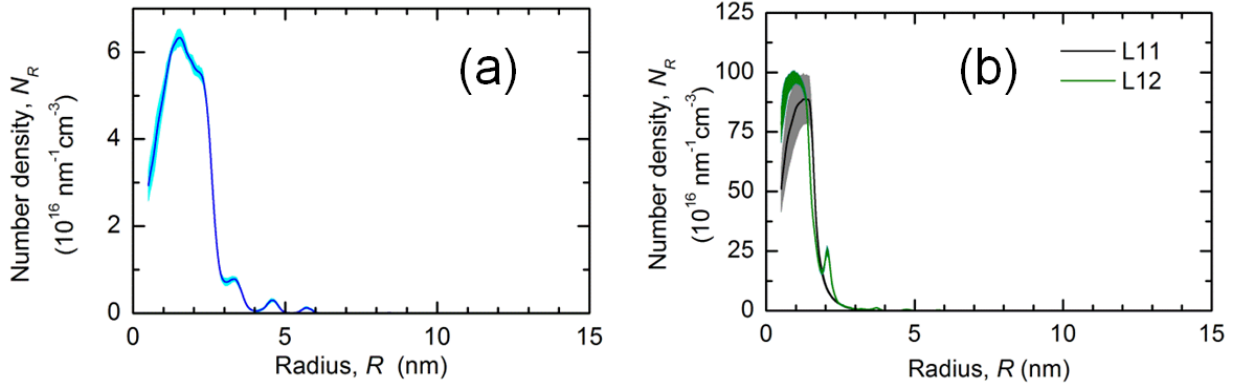


Fig. 8: Size distribution in terms of particle number density per radius increment for (a) the as-received condition of ODS Fe9Cr (L10) and (b) the as-received condition of ODS Fe14Cr (L12) and the yttria-free 14Cr reference (L11).

Table 3: Experimental results obtained for as-received ODS **Fe9Cr** extruded bar (lot L22-M1).

Technique	d_g (μm)	ρ (10^{14} m^{-2})	d_p (nm)	N_p (10^{22} m^{-3})	particle type (ratio Y-Ti-O)
Microstructure					
APT	-	-	5.1 ± 0.8	2.7 ± 0.5	close to 1-1-2
SANS	-	-	3.5 ± 0.2	12.3	consistent with 2-2-7 or 2-1-5
TEM		0.46 ± 0.1	(4.1 ± 0.9)	15 ± 4	
EBSD	1.19	-	-	-	-
Selected value	1	0.5	4	10	-

Table 4: Experimental results obtained for quenched and tempered ODS **Fe9Cr** extruded bar (lot L22-M1).

Technique	d_g (μm)	ρ (10^{14} m^{-2})	d_p (nm)	N_p (10^{22} m^{-3})	particle type (ratio Y-Ti-O)
Microstructure					
SANS*	-	-	3.5 ± 0.2	12.3	consistent with 2-2-7 or 2-1-5
TEM-1	0.25 **	-	(10 ± 5)	(0.1)	2-2-7
TEM-2		3.4 ± 1.0	4.7 ± 0.5	8 ± 2	
EBSD	0.46	-	-	-	-
Selected value	0.5	3	4	10	-

* SANS indicates equal size distributions for as-received and quenched + tempered ODS Fe9Cr

** Lath width

Table 5: Experimental results obtained for ODS Fe14Cr extruded bar (lot J27-M2).

Technique	d_g (μm)	ρ (10^{14} m^{-2})	d_p (nm)	N_p (10^{22} m^{-3})	particle type ratio Y-Ti-O
APT	-	-	2.8 ± 1.5	16.1 ± 1.7	close to 1-2-4
SANS*	-	-	2.3 ± 0.1	44 12	-
TEM-1	0.45	≈ 5	4	>2	-
TEM-2		**	2.2	32 ± 6	-
EBSL	0.51	-	-	-	-
Selected value	0.5	5	2.4	26	-

* The second value is the difference between ODS 14Cr extruded bar and the yttria-free Fe14Cr reference.

** Large spatial variations

3.4. APT results

Both ODS Fe9Cr and Fe14Cr extruded bars were characterized by APT. In each case, the global chemical composition and the characteristics of the nano-oxides were measured.

3.4.1. ODS Fe9Cr (as-received) extruded bar

The average chemical composition of the ODS Fe9Cr measured by APT is reported in Table 6 (including all features intercepted during APT analysis). The average composition is calculated from 3 APT dataset. Minimum and maximum concentrations of solutes from the different data set are also reported to give an estimation of the dispersion of the results. It appears that the distribution of elements from one volume to another is relatively homogeneous. A high concentration of C is measured in one of the volumes because a carbide enriched in Cr, W and Mn is partly intercepted. In comparison with the nominal (bulk) composition, the concentrations of Si, Mn, Ni, Cr and W are in good agreement with the expected ones. The levels of C, Ti, Y and O are very low compared to nominal ones, suggesting the presence of carbides and oxides with low number density (so not intercepted by APT analysis). Unexpectedly, low concentrations of Mo (~0.2 at.%) and traces of P, N, Al, V and Co (below 0.01%) are measured.

Table 6: APT (minimum, maximum and average values) and Bulk (chemical analysis) compositions of ODS Fe-9%Cr (at%, balance Fe). In addition to elements reported in the table, traces (< 0.01%) of N, Co, P, Al and V were also detected.

	C	Si	Mn	Ni	O	Cr	Y	Ti	W	Mo
APT minimum	0.011	0.58	0.25	0.22	0.039	7.91	0.004	0.023	0.23	

APT maximum	0.46	0.59	0.28	0.23	0.067	9.90	0.010	0.032	0.31	
APT average	0.042	0.58	0.27	0.23	0.058	9.67	0.01	0.026	0.30	0.023
Bulk	0.46	0.59	0.30	0.19	0.18	9.74	0.12	0.35	0.33	-

Two examples of volumes analyzed by APT are shown on Fig. 9. Small Y and Ti oxides are detected in all volumes. Their spatial distribution is heterogeneous. Indeed, the local number density varies from less than $0.2 \times 10^{22} \text{ m}^{-3}$ in particles free zones to about $6 \times 10^{22} \text{ m}^{-3}$. In average the number density is $(2.7 \pm 0.5) \times 10^{22} \text{ m}^{-3}$. Such distribution could be explained by the interaction of migrating grain boundary (GB) and Y and Ti oxides during ODS elaboration [31]. Most of the observed particles are located in matrix and only two are located at GB. There average sizes are 5.1 and 5.6 nm respectively. In average, the particle size is about $(5.1 \pm 0.8) \text{ nm}$ since a large majority is located in the matrix.

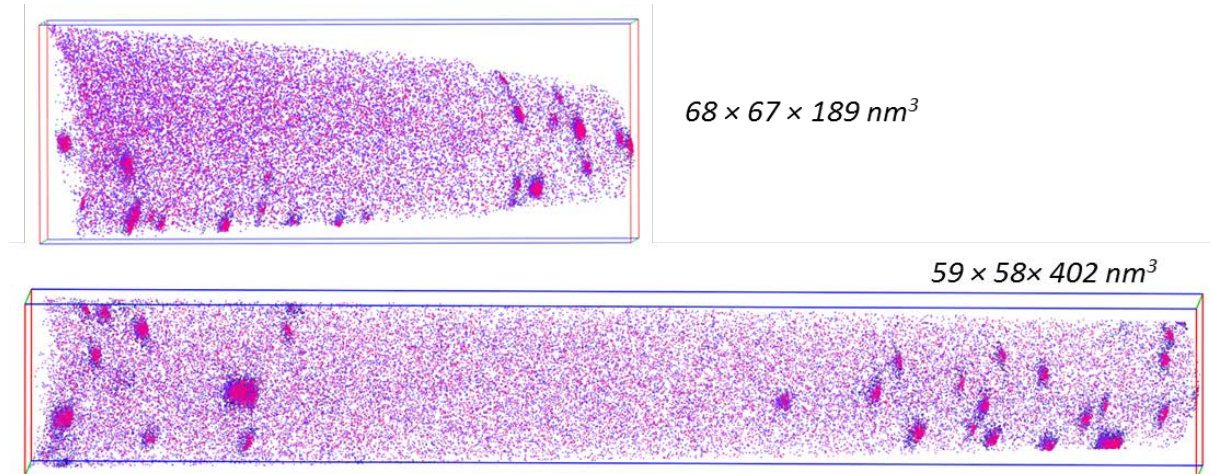


Fig. 9: Two examples of 3D reconstructions of the ODS Fe9Cr extruded bar. Y is in red, TiO molecular ions are in purple and O is in blue.

As far as the chemical composition of oxides is concerned, a high level of Fe and Cr is detected inside the particle. However, as it is said in section 2.2, the presence of these elements in particles is attributed to field evaporation artefacts. The chemical composition of the oxides located in the matrix (considering only Y, Ti and O) is $(22.4 \pm 0.9)\%Y - (22.3 \pm 0.9)\%Ti - (55.3 \pm 0.9)\%O$.

The APT results on ODS Fe9Cr extruded bar are summarized in Table 3.

3.4.2. ODS Fe14Cr extruded bar

The average chemical composition of the ODS Fe14Cr calculated from 4 APT dataset is reported in Table 7. Minimum and maximum concentrations of each solute

(depending of the dataset) are also reported. In comparison with the expected bulk composition, several impurities are detected (C, N, Co, P, Al, V), the level of Ni is too high and there is a lack of Y, Ti and O, suggesting the presence of a low number density of large oxides not intercepted by APT volumes. It also has to be noticed that the distribution of several solutes within the material is heterogeneous at a larger scale than typical APT volumes.

Table 7: APT (minimum, maximum and average values) and Bulk (chemical analysis) compositions of ODS Fe-14%Cr (at%, balance is Fe). In addition to elements reported in the table, traces (~0.01%) of N, Co, P, Al and V were also detected.

	C	Si	Mn	Ni	O	Cr	Y	Ti	W
APT minimum	0.002	0.57	0.31	0.21	0.043	12.7	0.004	0.016	0.14
APT maximum	0.082	0.95	0.33	0.25	0.40	15.5	0.071	0.15	0.29
APT average	0.026	0.67	0.32	0.24	0.13	13.35	0.017	0.05	0.20
Bulk	-	0.63	0.29	0.16	0.22	14.90	0.15	0.45	0.33

In the case of Y, Ti and O these strong fluctuations can be explained by an heterogeneous distribution of nano-oxides in the material. Two examples of the observed microstructures are shown on the Fig. 10. As it can be seen, nm-sized particles rich in Ti, Y and O are systematically observed. The largest ones are located at GB. In addition to largest Y and Ti oxides, the GBs are enriched in Cr. The average sizes of the particles located at GB and in the matrix are 3.7 and 2.5 nm respectively. The number density of particles at GB is about $4 \times 10^{24} \text{ m}^{-3}$. In the matrix, the particle distribution is strongly heterogeneous. Some volumes are almost free of particles whereas some others contain a high number density (from 1.2 to $53 \times 10^{22} \text{ m}^{-3}$). All in all, the average sizes and number density, considering particles at GB and inside grains, are $(2.8 \pm 1.5) \text{ nm}$ and $(16.1 \pm 1.8) \times 10^{22} \text{ m}^{-3}$, respectively.

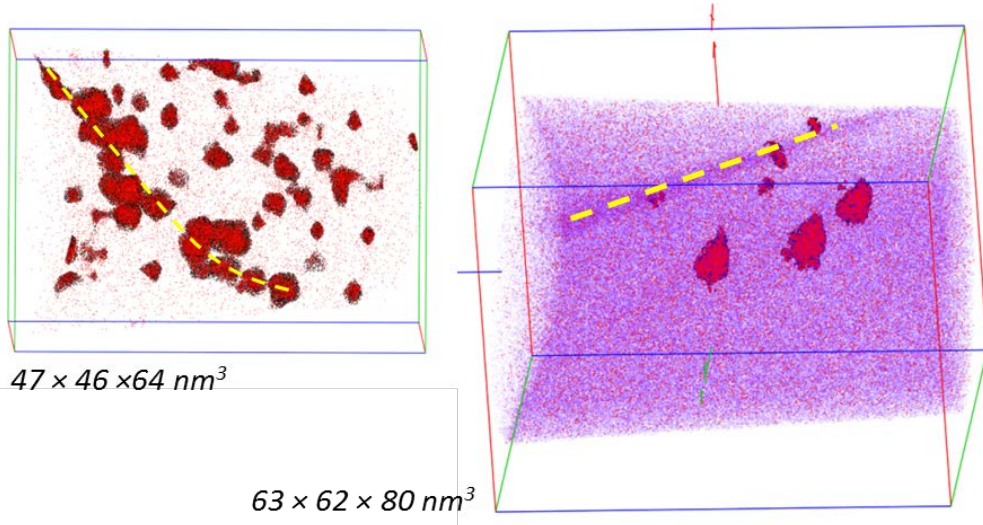


Fig. 10: Two examples of 3D reconstructions of the ODS Fe14Cr extruded bar. Cr is in purple, Y, Ti and O are in red and Fe is in black. Y-Ti oxides are highlighted. Grain boundaries are materialized by yellow dashed lines.

Here again, a high level of Fe and Cr is observed in the particles and is attributed to field evaporation artefacts. The particle stoichiometry considering only Ti, Y and O is nearly $(29.5 \pm 0.8)\%$ Ti, $(15.5 \pm 0.7)\%$ Y and $(55.0 \pm 0.9)\%$ O for particles inside matrix as well as particles at GB. The ratio Cr over Fe measured in the particles, as well as concentration profiles along particles long axis indicate that there are surrounded by Cr enriched shell. Characteristics of the particles, as measured by APT, are summarized in the Table 5.

In order to facilitate critical comparison between the different techniques, all the results introduced above are summarized in Tables 3 to 5.

3.5. Tensile properties

The main tensile properties for the studied ODS steels at room temperature are summarized in Table 8. Clearly, ODS Fe14Cr steel exhibits highest strength of all tested materials. In addition, the advantage of heat treatment on ODS Fe9Cr steel is apparent from the improvement in strength. Nevertheless, reduction in total elongation/ductility is obvious. All steels manifest significant strain hardening¹ with the highest for as-received ODS Fe9Cr F steel. Interestingly, under as-received condition ODS Fe9Cr steel exhibited a yield point phenomenon which indicates the presence of carbon in solid solution at interstitial sites [8], which is coherent with APT

¹ Strain hardening (%) = $\left(\frac{\text{Ultimate tensile stress} - \text{Yield stress}}{\text{Ultimate tensile stress}} \right) * 100$

measurements. The influence of temperature on tensile properties with microstructural evolution and fracture characteristics are reported [and discussed](#) separately, see Refs [8,27,32].

Table 8: Tensile data for the studied ODS steels at room temperature, for actual tensile curves and more see Refs [8,27].

Alloy	Yield stress (MPa)	Ultimate tensile strength (MPa)	Uniform elongation (%)	Total elongation (%)	Strain hardening (%)
ODS Fe9Cr F	740	903	10.3	20.9	18.1
ODS Fe9Cr TM	929	1052	2.7	7.6	11.7
ODS Fe14Cr F	1080	1126	9.1	20.9	4.1

3.6. Summary of additional reported results

One of the objectives of the present study is to gain insight from a comparison of measured yield stress with values calculated on the basis of simple models applied to measured microstructure characteristics. This kind of analysis can be strengthened considerably if the set of incorporated materials is extended in a dedicated manner. Therefore, we added a number of Fe-Cr model alloys, the reduced activation F/M steel Eurofer 97 (Eu97) and ODS Eurofer (ODS-Eu). For these materials, data sets are available from the reported literature with some gaps filled in the framework of the present study as detailed in Table 9. The average material parameters selected on the basis of Table 3 to 5 for ODS Fe9Cr and ODS Fe14Cr, respectively, within the present study are included for easier cross reference.

Table 9: Data sets for Fe-Cr model alloys, Eurofer 97 and ODS Eurofer reported in literature and average material parameters selected for ODS Fe9Cr and ODS Fe14Cr steels.

Alloy	Grain size d_g (μm) ¹⁾	Dislocation density ρ_d (10^{14} m^{-2})	Part. mean diameter d_p (nm)	Number density N_p (10^{22} m^{-3})	Yield stress σ_y (MPa)
Fe2.5Cr [33]	37	0.12	w/o	w/o	144
Fe5Cr [33]	10	0.58	w/o	w/o	206
Fe9Cr [33]	3	0.63	w/o	w/o	289
Fe12Cr [33]	3	0.55	w/o	w/o	349
Eu97 [34–36]	2	2.2	w/o	w/o	550
ODS-Eu [37–40]	0.5	7	3.8	11.5	1050
ODS Fe9Cr F	1	0.5	4	10	740
ODS Fe9Cr TM	0.5	3	4	10	929
ODS Fe14Cr F	0.5	5	2.4	26	1080

¹⁾ New estimations based on EBSD

4. Discussion

4.1. Microstructure features

A variety of experimental methods including TEM, EBSD, SANS and APT was applied to characterize the microstructure. As indicated in Table 3 to 5, the information gained from the application of these methods is partly complementary and partly overlaps. The complementarity is important for both a complete description of the microstructure and a microstructure-based “prediction” of the yield stress to be obtained. Indeed, no single technique alone is capable of providing a full characterization of the microstructure. The cases of overlap can be used to cross-check and additionally substantiate the derived microstructure parameters.

The type of microstructure was derived from optical metallography, EBSD and TEM. The results confirm that as-received ODS Fe9Cr, quenched and tempered ODS Fe9Cr and ODS Fe14Cr are essentially ferritic, tempered martensitic, and ferritic, respectively. Occasional appearances of ferrite in quenched and tempered ODS Fe9Cr and of martensite in ODS Fe14Cr were found but will be ignored in the further analysis. The appearance of martensite in ODS Fe14Cr can only be explained in terms of spatial variations of the Cr content locally falling below the extension of the γ -range in the phase diagram. The information gathered from different techniques on grain size is consistent for each of the materials. EBSD is favorable in extracting the grain size, because it combines sufficient spatial resolution and sufficient statistics. Taking into account the complete set of alloys listed in Table 9, the grain size varies over almost two orders of magnitude (from 0.5 to 37 μm) with the lower values associated to the ODS alloys (versus non-ODS) and to the martensitic microstructures (versus ferritic ones).

The dislocation density was derived exclusively on the basis of TEM. A considerable degree of heterogeneity was found with respect to the dislocation structure. However, rough estimates of the average dislocation density were derived from the analyses at different positions. Table 9 indicates that the dislocation density also varies over almost two orders of magnitude but with less obvious trends than for the grain size.

Information on the oxide nanoparticle distribution was derived from APT, TEM and SANS. The SANS results are distinguished by a probed volume (approximately 50 mm³) that is many order of magnitude larger than for TEM and APT and that allows macroscopically representative and statistically reliable size distributions to be obtained. On the other hand, SANS cannot resolve the composition of particles (in contrast to APT) nor discriminate between different types on nanoparticles of similar size. Taking into account the different sizes of the probed volumes and the observed heterogeneities of the spatial distribution of particles, the sizes and number densities of particles listed in Table 3 to 5 seem to be reasonably consistent. It is interesting to note that, based on SANS, quenching and tempering of ODS Fe9Cr did not change the size and number density of oxide nanoparticles.

4.2. Strengthening contributions

To understand the correlation between microstructures and yield stress, the microstructure-based strength calculation model is used to estimate the theoretical strength. It is first assumed here that the yield stress (σ_y) of the materials at room temperature can be given by a simple sum of strengthening contributions which is as follows:

$$\sigma_y = \sigma_0 + \sigma_s + \sigma_g + \sigma_d + \sigma_p \quad (1)$$

where σ_0 , σ_s , σ_g , σ_d and σ_p are the contributions from lattice friction, solid solution strengthening, grain size or Hall-Petch strengthening, dislocation forest strengthening and nanoparticles strengthening, respectively. Although pure linear summation according to Eq. (1) is an oversimplification, Eq. (1) may well serve as a road map to introduce the individual contributions separately. Moreover, it is interesting to see in section 4.3, to what extent more realistic models modify the prediction.

The lattice friction or Peierls-Nabarro stress (σ_0) is required to move a dislocation through the perfect lattice. As in here, all alloys considered have an iron lattice, the friction stress of single crystal pure iron is 53.9 MPa [41].

Solid solution strengthening (σ_s) includes both the interstitial strengthening from the carbon in solid solution and the substitution strengthening from all substitutional elements. However, with respect to the present alloys, interstitial strengthening will

have a negligible contribution since most of the carbon, present in appreciable amount only in ODS Fe9Cr steel, is already precipitated out in form of carbides. The strengthening effects of substitutional alloying elements in BCC iron matrix was experimentally obtained by Lacy and Gensamer [42], who reported a simple expression as:

$$\sigma_s = 0.00689 k X^n \quad (2)$$

where X is the equilibrium concentration of substitutional elements in atomic percent, $n = 0.75$ for all elements, and k is the strengthening coefficient measured by Lacy and Gensamer [42]. High values of k imply a large substitutional element effect. The main substitutional strengthening effects were calculated using Eq. 2 and are listed in Table 10 for each element. The total substitutional strengthening effects are introduced in Table 11 for each of the ODS steels and alloys.

Table 10: Strengthening from substitutional alloying elements dissolved in the matrix.

Elements	k	σ_s (ODS Fe9Cr) (MPa)	σ_s (ODS Fe14Cr) (MPa)
Cr	1400	53.2	71.2
W	11000	33.2	28.4
Si	11000	51.7	53.6
Mn	7000	19.6	18.1
Ni	6100	12.1	10.6
Total		169.7	181.9

In polycrystalline material, grain size plays an important role on mechanical properties. Grain size or Hall-Petch strengthening (σ_g) expresses the influence of grain boundaries on dislocation behavior. Indeed, dislocations are gradually stacked at grain boundaries and form pile-ups until they reach the threshold to pass to the next grain. As suggested in [12], this strengthening contribution can be estimated as:

$$\sigma_g = \alpha_g G \sqrt{\frac{b}{d_g}} \quad (3)$$

Here $\alpha_g = 0.2$ [12], G is the shear modulus (= 85 GPa at room temperature [43], measured value for ODS high-Cr steels), b is the Burgers vector (= 0.248 nm, assuming all dislocations have a Burgers vector of the type $\frac{1}{2} \langle 111 \rangle$) and d_g is the mean grain size. The estimated values of Hall-Petch strengthening for the studied ODS steels and alloys are listed in Table 11.

Dislocation forest strengthening (σ_d) is due to the interaction between dislocations when a mobile dislocation interacts with another one which goes across its gliding plane. The contribution from dislocations strengthening can be estimated by Bailey-Hirsch relationship [44], which is widely accepted as:

$$\sigma_d = \alpha_d M G b \sqrt{\rho_d} \quad (4)$$

where α_d is an obstacle strength for dislocations by dislocations (= 1/3 according to [12]), M is the Taylor factor that was recommended as 3.06 for most polycrystalline BCC metals [45] and ρ_d is the dislocation density. The estimated values of dislocation strengthening for the studied ODS steels and alloys are listed in Table 11.

Particle strengthening (σ_p) is due to the dispersed nano-oxide particles which act as impenetrable obstacles for dislocations glide. Several authors suggested detailed equations for calculating this contribution, which were partly based on knowledge or assumptions about the dislocation-particle interaction mechanism [46–48]. For the present purpose, this degree of detailedness seems to be inappropriate, since different interaction mechanisms may be assumed to operate simultaneously depending upon various factors such as particle type, their degree of coherency etc. It is therefore reasonable to use the simplest scaling equation with an empirical constant. One such equation based on the dispersed barrier hardening concept, after the original formulation of Seeger [49], is used often [14] and is as follows [50]:

$$\sigma_p = \alpha_p M G b \sqrt{N_p d_p} \quad (5)$$

where α_p is the obstacle strength for oxide nano-particles (= 1/3 which may vary between 0.1 and 0.5 depending on particle type and degree of coherency, mean value), N_p is the number density of nano-oxide particles and d_p is the mean particle diameter. The estimated particle strengthening for the studied ODS steels are briefed in Table 11.

From Table 11, it is evident that the increasing order of strengthening components for ODS Fe9Cr F is $\sigma_0 < \sigma_d < \sigma_s < \sigma_g < \sigma_p$, for ODS Fe9Cr TM is $\sigma_0 < \sigma_s < \sigma_d < \sigma_g < \sigma_p$ and for ODS Fe14Cr F is $\sigma_0 < \sigma_s < \sigma_g < \sigma_d < \sigma_p$. Therefore, for the studied ODS steels particle strengthening provides a major contribution to the measured room temperature yield stress, which is more than 45% in all three cases. This is in

~~contradiction with the previous studies [11,12,14,17], for more see section 1.~~ In addition, dislocation forest and grain size strengthening are also dominant contributors to the yield stress. The dominating share of particle contributions to the room temperature yield stress are in contradiction with previous studies [11,12,14,17], where based on distinct microstructural characteristics (fined grained, high dislocation density and particle's larger size, their lower density and them being coherent), dislocation forest and/or grain size strengthening contributions are either comparable or higher than the particle strengthening. However, it is important to note that here calculated strengthening contributions are only room temperature specific. And as investigated in detail by Kim et al. MSEA 2013, the roles of individual strengthening mechanisms alter significantly with temperature. Clearly, for ODS Fe9Cr TM steel, Hall-Petch strengthening is greater than dislocation forest strengthening. On the contrary, dislocation forest strengthening is higher than the Hall-Petch strengthening for ODS Fe14Cr steel. This is due to fact that even if both steels manifest similar average grain size; the dislocation density is slightly higher in ODS Fe14Cr steel than in heat-treated ODS Fe9Cr TM steel.

4.3. Comparison of the measured and calculated yield stress

The yield stress values of the studied alloys tentatively estimated according to Eq. 1 are listed in Table 11 along with corresponding data for the additional alloys reported in the literature. Obviously, the linear summation of all contribution leads to a considerable overestimation of the yield stress, which is 25-34% higher than the measured yield stress for the ODS alloys of this study. An overestimation of the yield stress is also observed for the binary Fe-Cr alloys, Eurofer 97 and ODS-Eurofer, which were additionally introduced into the analysis.

Table 11: Various strengthening contributions along with the calculated and experimental yield stresses (all in MPa). The materials investigated in this study are placed in the lower part of the table; the results obtained for the additional alloys from the literature are listed in the upper part.

Alloy	σ_s ¹⁾	σ_g	σ_d	σ_p	$\sigma_{y,th}$ (Eq.1)	$\sigma_{y,th}$ (Eq. 6)	$\sigma_{y,th}$ (Eq. 7)	$\sigma_{y,exp}$
Fe2.5Cr [33]	19.6	44.0	73.0	0	191	191	117	144
Fe5Cr [33]	31.9	84.7	160.5	0	331	331	245	206
Fe9Cr [33]	49.8	154.6	167.3	0	426	426	322	289
Fe12Cr [33]	63.5	154.6	156.3	0	428	428	311	349
Eu97 [34–36]	126.6	189.3	312.7	0	683	683	502	550
ODS-Eu [37–40]	126.8	378.6	557.7	440.7	1558	1270	1089	1050

ODS Fe9Cr F	169.7	267.7	149.1	421.6	1064	940	715	740
ODS Fe9Cr TM	169.7	378.6	365.1	421.6	1391	1162	936	929
ODS Fe14Cr F	181.9	378.6	471.4	526.6	1614	1323	1085	1080

¹⁾ $\sigma_0 = 53.9 \text{ MPa}$ for Eqs. 1 and 6 for all alloys (not included in the table)

In general, the observed overestimation may be due to either the type of superposition or the overestimation of (one or more) individual strengthening contributions. Both options are considered below.

Pythagorean superposition of the contributions from dislocations and particles was suggested by several authors [48,51–53] to be more appropriate. Kamikawa et al. [53] also reported an overestimation of the yield stress for low-Cu steels with nano-precipitates in the case of assumed linear superposition and substantiate Pythagorean superposition by the small spacing of dislocations and precipitates, both of which act as short range obstacles. This is because the mean spacings of dislocations and nanoparticles are comparable while grain size is an order of magnitude larger, and the motion of dislocations would be impeded by both dislocations and oxide particles. Therefore, the strengthening contributions from dislocations and particles ought to be mixed together which cannot simply be additive. Queyreau et al. [48] used dislocation dynamics simulations to show that Pythagorean superposition is appropriate for the combination of both contributions in the underlying model. These arguments led us to replace Eq. 1 by Eq. 6. Furthermore, concerning ODS steels, such superposition has been used several times [16–18]. The yield stress values calculated according to Eq. 6 are included in Table 11.

$$\sigma_y = \sigma_0 + \sigma_s + \sigma_g + \sqrt{\sigma_d^2 + \sigma_p^2} \quad (6)$$

It has been foreseeable that Pythagorean instead of linear superposition will reduce (or remove) the overestimation. However, comparison of the calculated and measured yield stress shows that there is still a significant though smaller overestimation of the yield stress for all alloys, see Fig. 11a. In order to identify the most probable sources of overestimation, it is helpful to analyze the trend of the residuals shown in Fig. 11b.

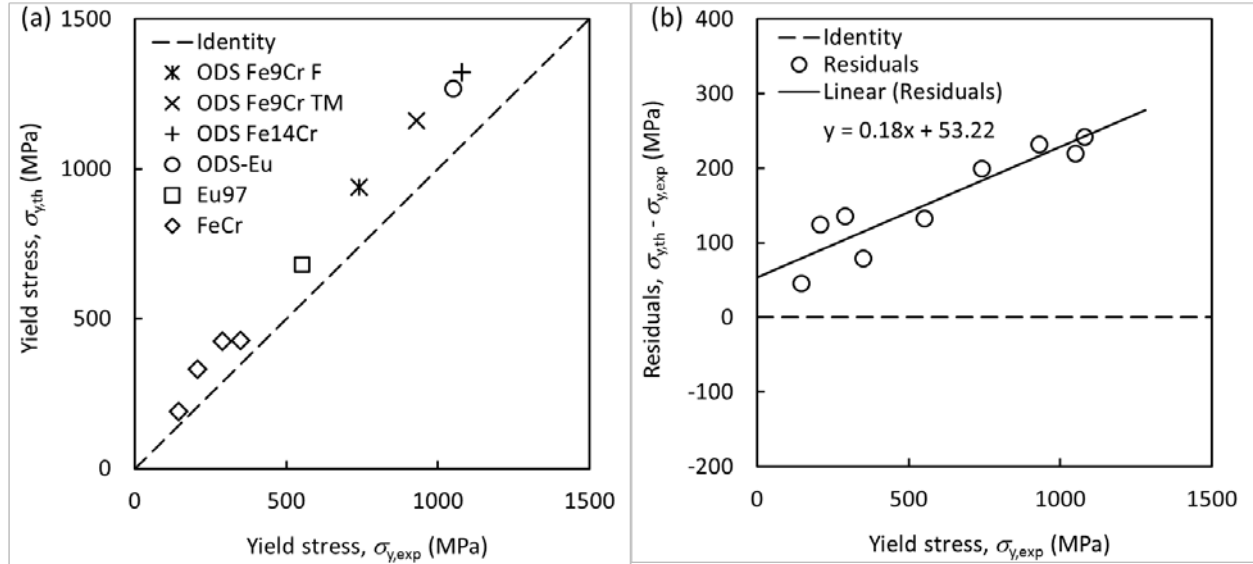


Fig. 11: (a) Yield stress calculated according to Eq. 6 versus experimental yield stress and (b) residuals versus experimental yield stress for the studied alloys.

Fig. 11b clearly shows that the residuals are composed of an offset, which is independent of the yield stress of the alloys, and a part (trend) that increases with increasing yield stress. The offset led us to try to remove the friction stress from Eq. 6. Indeed, the friction stress is the only contribution to the total yield stress that is conceptually equal for all alloys. Moreover, the observed offset of 53 MPa approximately agrees with the considered friction stress of 53.9 MPa. The following arguments substantiate the elimination of the friction stress:

1. The friction stress depends on the type of dislocation, slip system and temperature. In situations (not too low temperatures, screw dislocations), where the Peierls barrier is overcome by a kink-pair mechanism, the friction stress is close to zero [54,55].
2. Dislocation unpinning from an obstacle (e.g. oxide nanoparticle) is an instability not reflected well by the balance of forces. The height of the Peierls barrier may be irrelevant for the critical unpinning stress.
3. In literature, smaller values of friction stress, e.g. 30 MPa [56], have also been reported.

In addition to the friction stress, solid solution strengthening can lead to overestimation exhibiting a trend. Lower solid solution strengthening than predicted by Eq. 2 (or even its absence) may be justified as follows:

1. Not all Cr and W will contribute to solid solution strengthening, since Cr- and W-containing grain boundary carbides and/or oxide nano-particles are often observed. These may not alter particle strengthening significantly but reduce Cr and W in solution with respect to the analysis.
2. The contribution of Cr to solid solution strengthening is sometimes reported to be smaller than predicted by the expression used here or even negative [57], the latter corresponding to solid solution softening.
3. Other cases of solid solution softening (e.g. by Si) under certain conditions are reported by Caillard [58].
4. Similar as for the friction stress, solid solution strengthening may also be irrelevant for the critical unpinning stress.

Hence, in order to empirically improve the estimation of the yield stress, only dominant contributors (σ_g , σ_d and σ_p) are considered. The contribution from friction stress and solid solution strengthening are ruled out to reduce both the offset and the trend of the residuals observed in Fig. 11b. It is interesting to note that other authors also omitted friction stress and solid solution strengthening contributions for high-strength materials and still found good agreement with experimental values, for example see Ref. [12,59]. This conceptualizes into an equation of the following type:

$$\sigma_y = \sigma_g + \sqrt{\sigma_d^2 + \sigma_p^2} \quad (7)$$

The yield stress values calculated according to Eq. 7 are listed in Table 11. The comparison of the calculated and measured yield stress shows that Eq.7 is favorable and describes the whole set of ODS and non-ODS Fe-Cr steels and alloys reasonably well, see Fig. 12a. Moreover, an insignificant offset and trend of residuals are apparent in Fig. 12b. Furthermore, suitability of the choice of model parameters and determination of microstructure parameters are broadly confirmed.

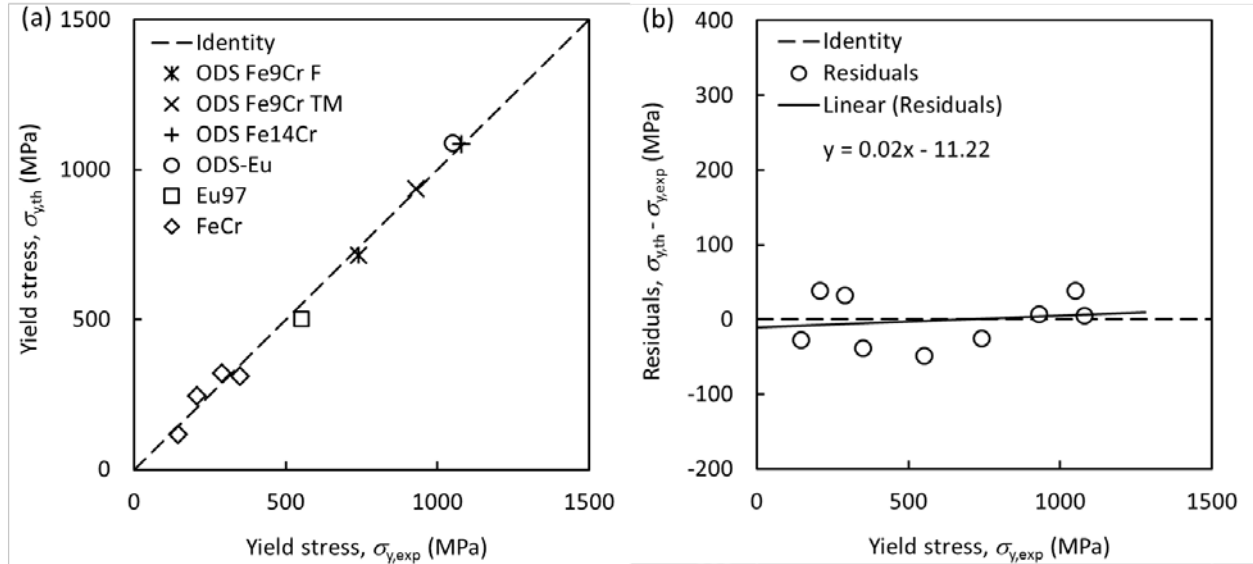


Fig. 12: (a) Yield stress calculated according to Eq. 7 versus experimental yield stress and (b) residuals versus experimental yield stress for the studied alloys.

The good fit of Eq. 7 with the measured yield stress must not be misinterpreted as to represent a strict proof of its absolute validity. For example, a small modification of the model parameters with the value of $\alpha_g = 0.157$ [53] instead of the selected value $\alpha_g = 0.2$ [12] in Eq. 3 and 33% of the full calculated solid solution strengthening instead of 0% in Eq. 7 will give rise to a similar quality of the fit. The validity of both variants of the model cannot be distinguished on the basis of the present framework. Another example is related to the possible inclusion of Hall-Petch strengthening in the Pythagorean-superposition part of Eq. 6, which contradicts the reasoning of [Kamikawa et al.] but complies with [Ferguson et al.]. This kind of superposition model yields a slightly worse fit and a larger magnitude of the trend (-0.09 versus 0.02) than Eq. 7, but again cannot be strictly ruled out.

4.4. Basis for evaluating irradiation-induced strength changes

An important consequence of the empirically identified model, Eq. 7 along with Eqs. 3 to 5, is related to the analysis of the irradiation-induced yield stress increase, which is not considered here but represents an issue for nuclear structural materials such as ODS steels. Usually, linear superposition between the yield stress of the unirradiated reference material and the irradiation-induced yield stress increase is considered. Although often not explicitly stated, this manifests itself in the very use of the irradiation-induced yield stress increase, $\Delta\sigma_y = \sigma_{\text{irr}} - \sigma_{\text{unirr}}$ [60]. Sometimes,

Pythagorean superposition is introduced as an alternative option. The following reasoning shows that neither linear nor Pythagorean superposition is fully compatible with Eq. 7.

Let us assume a situation, where irradiation-induced dislocation loops, nanovoids and/or defect-solute clusters form. These compete with the particles of the unirradiated reference materials represented in Eq. 7 as dislocation obstacles. The resulting yield stress is:

$$\sigma_{y,irr} = \sigma_g + \sqrt{\sigma_d^2 + \sigma_{p,unirr}^2 + \sigma_{p,irr}^2} \quad (8)$$

Comparison of Eqs. 7 and 8 shows that both

$$\sigma_{y,irr} - \sigma_{y,unirr} \neq \sigma_{p,irr} \quad (9)$$

and

$$\sigma_{y,irr}^2 - \sigma_{y,unirr}^2 \neq \sigma_{p,irr}^2 \quad (10)$$

are applicable, which expresses the incompatibility indicated above. In conclusion, special attention has to be paid to the superposition rule for the irradiation-induced yield stress increase. This requires knowledge about the superposition rule for the hardening contributions of the unirradiated material as provided in the present study.

5. Summary and conclusions

Microstructure characterization and [room temperature](#) strengthening mechanisms of ODS Fe9Cr and Fe14Cr extruded bars were investigated. A summary and conclusions are given below:

1. Reasonable agreement for the microstructural characterization results using different techniques was observed.
2. The differences can be explained in terms of differing details of the techniques such as detection limits or sampled volumes.
3. Complementarity of methods guarantees sufficiently complete description of the microstructures.
4. Among various strengthening sources, particle strengthening provides a major contribution to the measured [room temperature](#) yield stress, which is more than 45% in the studied ODS steels. In addition, dislocation forest and grain

size strengthening are also dominant contributors. However, it is noteworthy that here calculated strengthening contributions are only room temperature specific and their roles will alter significantly with temperature.

4.5. The dominating share of particle contributions to the room temperature yield stress are in contradiction with previous studies [11,12,14,17], where based on the distinct microstructural characteristics (fined grained, high dislocation density as well as larger size, lower density and coherency of the particles), dislocation forest and grain size strengthening contributions are either comparable or higher than the particle strengthening.

5.6. Linear superposition of all strengthening contributions resulted in considerable overestimation of yield stress.

6.7. In order to remove the offset of the calculated versus measured yield stress and to remove the trend of the residuals to an insignificantly small level, it was necessary to skip friction stress and solid solution strengthening. Arguments in favor of that are provided. Our results provide additional evidence that the friction stress of single crystals and low-yield-stress materials is irrelevant for dislocations overcoming a high number density of obstacles.

7.8. Grain size strengthening along with Pythagorean summation of dislocation forest strengthening and particle strengthening describes the whole set of ODS and non-ODS Fe-Cr steels and alloys reasonably well. This is particularly remarkable since the whole set of alloys spans an order of magnitude or more in terms of grain size, dislocation density, particle density and yield stress.

8.9. Furthermore, suitability of the choice of model parameters and determination of microstructure parameters are broadly confirmed.

The result serves as an appropriate basis for the evaluation of irradiation-induced strengthening in ongoing work. Indeed, the applicability of Eq. 7 predicts that irradiation-induced nano-features will have to be incorporated in the σ_p term under the square-root. This means that neither a pure linear nor a pure Pythagorean superposition of the irradiation-induced strengthening with the yield stress of the unirradiated reference materials would be appropriate.

Acknowledgement

This work was carried out under the financial support of European atomic energy community (Euratom) 7th Framework Programme FP7-Fission-2013 for Research and Technological Development under the Grant agreement no. 604862 (MatISSE project) and in the framework of the EERA (European Energy Research Alliance) Joint Programme on Nuclear Materials. The SANS experiment was performed at HZB Berlin. We would like to thank U. Keiderling for support.

References

- [1] R.L. Klueh, J.P. Shingledecker, R.W. Swindeman, D.T. Hoelzer, Oxide dispersion-strengthened steels: A comparison of some commercial and experimental alloys, *J. Nucl. Mater.* 341 (2005) 103–114. doi:10.1016/j.jnucmat.2005.01.017.
- [2] S. Ukai, M. Fujiwara, Perspective of ODS alloys application in nuclear environments, *J. Nucl. Mater.* 307–311 (2002) 749–757. doi:10.1016/S0022-3115(02)01043-7.
- [3] G.R. Odette, M.J. Alinger, B.D. Wirth, Recent Developments in Irradiation-Resistant Steels, *Annu. Rev. Mater. Res.* 38 (2008) 471–503. doi:10.1146/annurev.matsci.38.060407.130315.
- [4] S. Ukai, T. Narita, A. Alamo, P. Parmentier, Tube manufacturing trials by different routes in 9CrW-ODS martensitic steels, *J. Nucl. Mater.* 329–333 (2004) 356–361. doi:10.1016/j.jnucmat.2004.04.082.
- [5] P. Dubuisson, Y. De Carlan, V. Garat, M. Blat, ODS Ferritic/martensitic alloys for Sodium Fast Reactor fuel pin cladding, *J. Nucl. Mater.* 428 (2012) 6–12. doi:10.1016/j.jnucmat.2011.10.037.
- [6] J.J. Huet, Preparation and Properties of oxide dispersion-strengthened ferritic alloys, *Met. Powder Rep.* 40 (1985) 155–158.
- [7] D.K. Mukhopadhyay, F.H. Froes, D.S. Gelles, Development of oxide dispersion strengthened ferritic steels for fusion, *J. Nucl. Mater.* 258–263 (1998) 1209–1215. doi:10.1016/S0022-3115(98)00188-3.
- [8] A. Chauhan, D. Litvinov, Y. de Carlan, J. Aktaa, Study of the deformation and damage mechanisms of a 9Cr-ODS steel: Microstructure evolution and fracture characteristics, *Mater. Sci. Eng. A.* 658 (2016) 123–134. doi:10.1016/j.msea.2016.01.109.
- [9] S.J. Zinkle, L.L. Snead, Designing Radiation Resistance in Materials for Fusion Energy, *Annu. Rev. Mater. Res.* 44 (2014) 241–267. doi:10.1146/annurev-matsci-070813-113627.
- [10] R.L. Klueh, D.R. Harries, High-Chromium Ferritic and Martensitic Steels for Nuclear Applications, ASTM International, 100 Barr Harbor Drive, PO Box

C700, West Conshohocken, PA 19428-2959, 2001. doi:10.1520/MONO3-EB.

- [11] J.H. Schneibel, M. Heilmaier, W. Blum, G. Hasemann, T. Shanmugasundaram, Temperature dependence of the strength of fine- and ultrafine-grained materials, *Acta Mater.* 59 (2011) 1300–1308. doi:10.1016/j.actamat.2010.10.062.
- [12] M. Praud, F. Mompiou, J. Malaplate, D. Caillard, J. Garnier, A. Steckmeyer, et al., Study of the deformation mechanisms in a Fe–14% Cr ODS alloy, *J. Nucl. Mater.* 428 (2012) 90–97. doi:10.1016/j.jnucmat.2011.10.046.
- [13] M. Song, C. Sun, J. Jang, C.H. Han, T.K. Kim, K.T. Hartwig, et al., Microstructure refinement and strengthening mechanisms of a 12Cr ODS steel processed by equal channel angular extrusion, *J. Alloys Compd.* 577 (2013) 247–256. doi:10.1016/j.jallcom.2013.04.198.
- [14] J.H. Kim, T.S. Byun, D.T. Hoelzer, C.H. Park, J.T. Yeom, J.K. Hong, Temperature dependence of strengthening mechanisms in the nanostructured ferritic alloy 14YWT: Part II—Mechanistic models and predictions, *Mater. Sci. Eng. A.* 559 (2013) 111–118. doi:10.1016/j.msea.2012.08.041.
- [15] R. DiDomizio, S. Huang, L. Dial, J. Ilavsky, M. Larsen, An Assessment of Milling Time on the Structure and Properties of a Nanostructured Ferritic Alloy (NFA), *Metall. Mater. Trans. A.* 45 (2014) 5409–5418. doi:10.1007/s11661-014-2521-9.
- [16] B. Mouawad, X. Boulnat, D. Fabrègue, M. Perez, Y. de Carlan, Tailoring the microstructure and the mechanical properties of ultrafine grained high strength ferritic steels by powder metallurgy, *J. Nucl. Mater.* 465 (2015) 54–62. doi:10.1016/j.jnucmat.2015.05.053.
- [17] J. Shen, Y. Li, F. Li, H. Yang, Z. Zhao, S. Kano, et al., Microstructural characterization and strengthening mechanisms of a 12Cr-ODS steel, *Mater. Sci. Eng. A.* 673 (2016) 624–632. doi:10.1016/j.msea.2016.07.030.
- [18] M. Dadé, J. Malaplate, J. Garnier, F. De Geuser, F. Barcelo, P. Wident, et al., Influence of microstructural parameters on the mechanical properties of oxide dispersion strengthened Fe-14Cr steels, *Acta Mater.* (2017). doi:10.1016/j.actamat.2017.01.026.
- [19] MatISSE, <http://www.fp7-matisse.eu/>.
- [20] A. Michaux, L. Malerba, A. Bohnstedt, C. Mingazzini, M. Serrano, K.-F. Nilsson, et al., Materials' innovations for a safe and sustainable nuclear in Europe, in: NEA Int. Work. Struct. Mater. Innov. Nucl. Syst., Manchester, UK, 2016.
- [21] U. Keiderling, A. Wiedenmann, New SANS instrument at the BER II reactor in Berlin, Germany, *Phys. B Condens. Matter.* 213–214 (1995) 895–897. doi:10.1016/0921-4526(95)00316-2.
- [22] U. Keiderling, The new “BerSANS-PC” software for reduction and treatment of small angle neutron scattering data, *Appl. Phys. A Mater. Sci. Process.* 74

(2002) s1455–s1457. doi:10.1007/s003390201561.

- [23] A. Wagner, F. Bergner, A. Ulbricht, C.D. Dewhurst, Small-angle neutron scattering of low-Cu RPV steels neutron-irradiated at 255°C and post-irradiation annealed at 290°C, *J. Nucl. Mater.* 441 (2013) 487–492. doi:10.1016/j.jnucmat.2013.06.032.
- [24] S. Martelli, P.E. Di Nunzio, Particle Size Distribution of Nanospheres by Monte Carlo Fitting of Small Angle X-Ray Scattering Curves, *Part. Part. Syst. Charact.* 19 (2002) 247–255. doi:10.1002/1521-4117(200208)19:4<247::AID-PPSC247>3.0.CO;2-8.
- [25] W. Lefebvre-Ulrikson, F. Vurpillot, X. Sauvage, *Atom probe tomography : put theory into practice*, Academic Press, 2016.
- [26] C. Hatzoglou, Quantification et correction des biais inhérents à l'analyse par sonde atomique tomographique des nanoparticules d'un acier ODS : Application à l'étude de leur formation et à leur comportement sous irradiation, Université de Rouen, 2015.
- [27] M. Serrano, M. Hernández-Mayoral, A. García-Junceda, Microstructural anisotropy effect on the mechanical properties of a 14Cr ODS steel, *J. Nucl. Mater.* 428 (2012) 103–109. doi:10.1016/j.jnucmat.2011.08.016.
- [28] A. García-Junceda, M. Hernández-Mayoral, M. Serrano, Influence of the microstructure on the tensile and impact properties of a 14Cr ODS steel bar, *Mater. Sci. Eng. A.* 556 (2012) 696–703. doi:10.1016/j.msea.2012.07.051.
- [29] M. Serrano, A. García-Junceda, R. Hernández, M.H. Mayoral, On anisotropy of ferritic ODS alloys, *Mater. Sci. Technol.* 30 (2014) 1664–1668. doi:10.1179/1743284714Y.0000000552.
- [30] I. Hilger, F. Bergner, A. Ulbricht, A. Wagner, T. Weißgärber, B. Kieback, et al., Investigation of spark plasma sintered oxide-dispersion strengthened steels by means of small-angle neutron scattering, *J. Alloys Compd.* 685 (2016) 927–935. doi:10.1016/j.jallcom.2016.06.238.
- [31] N. Sallez, C. Hatzoglou, F. Delabrouille, D. Sornin, L. Chaffron, M. Blat-Yrieix, et al., Precipitates and boundaries interaction in ferritic ODS steels, *J. Nucl. Mater.* 472 (2016) 118–126. doi:10.1016/j.jnucmat.2016.01.021.
- [32] D. Litvinov, A. Chauhan, J. Aktaa, Microstructural evolution of 9Cr-ODS steel during high temperature deformation, in: *Eur. Microsc. Congr. 2016 Proc.*, Wiley-VCH Verlag GmbH & Co. KGaA, Weinheim, Germany, 2016: pp. 850–851. doi:10.1002/9783527808465.EMC2016.6095.
- [33] M. Matijasevic, A. Almazouzi, Effect of Cr on the mechanical properties and microstructure of Fe–Cr model alloys after n-irradiation, *J. Nucl. Mater.* 377 (2008) 147–154. doi:10.1016/j.jnucmat.2008.02.061.
- [34] C. Heintze, F. Bergner, M. Hernández-Mayoral, R. Köbler, G. Müller, A. Ulbricht, Irradiation hardening of Fe–9Cr-based alloys and ODS Eurofer: Effect

of helium implantation and iron-ion irradiation at 300 °C including sequence effects, *J. Nucl. Mater.* 470 (2016) 258–267.
doi:10.1016/j.jnucmat.2015.12.041.

- [35] A. Zeman, L. Debarberis, J. Kočík, V. Slugeň, E. Keilová, Microstructural analysis of candidate steels pre-selected for new advanced reactor systems, *J. Nucl. Mater.* 362 (2007) 259–267. doi:10.1016/j.jnucmat.2007.01.068.
- [36] M. Matijasevic, E. Lucon, A. Almazouzi, Behavior of ferritic/martensitic steels after n-irradiation at 200 and 300°C, *J. Nucl. Mater.* 377 (2008) 101–108.
doi:10.1016/j.jnucmat.2008.02.063.
- [37] R. Lindau, A. Möslang, M. Schirra, P. Schlossmacher, M. Klimenkov, Mechanical and microstructural properties of a hipped RAFM ODS-steel, *J. Nucl. Mater.* 307–311 (2002) 769–772. doi:10.1016/S0022-3115(02)01045-0.
- [38] I. Kuběna, J. Polák, T.P. Plocinski, C. Hébert, V. Škorík, T. Kruml, Microstructural stability of ODS steels in cyclic loading, *Fatigue Fract. Eng. Mater. Struct.* 38 (2015) 936–947. doi:10.1111/ffe.12284.
- [39] C. Heintze, F. Bergner, A. Ulbricht, M. Hernández-Mayoral, U. Keiderling, R. Lindau, et al., Microstructure of oxide dispersion strengthened Eurofer and iron–chromium alloys investigated by means of small-angle neutron scattering and transmission electron microscopy, *J. Nucl. Mater.* 416 (2011) 35–39.
doi:10.1016/j.jnucmat.2010.11.102.
- [40] N.V. Luzginova, H.S. Nolles, P. ten Pierick, T. Bakker, R.K. Mutnuru, M. Jong, et al., Irradiation response of ODS Eurofer97 steel, *J. Nucl. Mater.* 428 (2012) 192–196. doi:10.1016/j.jnucmat.2011.08.030.
- [41] F.B. Pickering, *Physical Metallurgy and the design of steels*, illustrate, Applied Science Publishers, 1978.
- [42] C.E. Lacy, M. Gensamer, The tensile properties of alloyed ferrites, *Trans. Am. Soc. Met.* 32 (1944) 88.
- [43] F. Bergner, Elastic properties of Fe-Cr and ODS Fe-Cr alloys, in: *Eur. Congr. Exhib. Adv. Mater. Process.*, Sevilla, Spain, 2013.
doi:10.13140/RG.2.1.3783.5281.
- [44] J.E. Bailey, P.B. Hirsch, The dislocation distribution, flow stress, and stored energy in cold-worked polycrystalline silver, *Philos. Mag.* 5 (1960) 485–497.
doi:10.1080/14786436008238300.
- [45] R.E. Stoller, S.J. Zinkle, On the relationship between uniaxial yield strength and resolved shear stress in polycrystalline materials, *J. Nucl. Mater.* 283–287 (2000) 349–352. doi:10.1016/S0022-3115(00)00378-0.
- [46] K.C. Russell, L.. Brown, A dispersion strengthening model based on differing elastic moduli applied to the iron-copper system, *Acta Metall.* 20 (1972) 969–974. doi:10.1016/0001-6160(72)90091-0.
- [47] D.J. Bacon, U.F. Kocks, R.O. Scattergood, The effect of dislocation self-

- interaction on the orowan stress, *Philos. Mag.* 28 (1973) 1241–1263. doi:10.1080/14786437308227997.
- [48] S. Queyreau, G. Monnet, B. Devincre, Orowan strengthening and forest hardening superposition examined by dislocation dynamics simulations, *Acta Mater.* 58 (2010) 5586–5595. doi:10.1016/j.actamat.2010.06.028.
- [49] A.K. Seeger, On the theory of radiation damage and radiation hardening, in: Proc. Second United Nations Int. Conf. Peac. Uses At. Energy, Vol. 6, Geneva, 1958: pp. 250– 273.
- [50] G.S. Was, Irradiation Hardening and Deformation, in: Fundam. Radiat. Mater. Sci., Springer Berlin Heidelberg, Berlin, Heidelberg, 2007: pp. 581–642. doi:10.1007/978-3-540-49472-0_12.
- [51] A.J.E. Foreman, M.J. Makin, Dislocation movement through random arrays of obstacles, *Can. J. Phys.* 45 (1967) 511–517. doi:10.1139/p67-044.
- [52] E. Hornbogen, E.A. Starke, Overview no. 102 Theory assisted design of high strength low alloy aluminum, *Acta Metall. Mater.* 41 (1993) 1–16. doi:10.1016/0956-7151(93)90334-O.
- [53] N. Kamikawa, K. Sato, G. Miyamoto, M. Murayama, N. Sekido, K. Tsuzaki, et al., Stress-strain behavior of ferrite and bainite with nano-precipitation in low carbon steels, *Acta Mater.* 83 (2015) 383–396. doi:10.1016/j.actamat.2014.10.010.
- [54] D. Brunner, J. Diehl, The use of stress-relaxation measurements for investigations on the flow stress of α -iron, *Phys. Status Solidi.* 104 (1987) 145–155. doi:10.1002/pssa.2211040110.
- [55] Z. Chen, Modelling the plastic deformation of iron, Karlsruhe Institute of Technology, 2013. doi:10.5445/KSP/1000032216.
- [56] Q. Li, Modeling the microstructure–mechanical property relationship for a 12Cr–2W–V–Mo–Ni power plant steel, *Mater. Sci. Eng. A.* 361 (2003) 385–391. doi:10.1016/S0921-5093(03)00565-3.
- [57] F.B. Pickering, Structure-Property Relationships in Steels, in: Mater. Sci. Technol., Wiley-VCH Verlag GmbH & Co. KGaA, Weinheim, Germany, 2006. doi:10.1002/9783527603978.mst0062.
- [58] D. Caillard, A TEM *in situ* study of alloying effects in iron. I—Solid solution softening caused by low concentrations of Ni, Si and Cr, *Acta Mater.* 61 (2013) 2793–2807. doi:10.1016/j.actamat.2013.01.048.
- [59] A. Steckmeyer, M. Praud, B. Fournier, J. Malaplate, J. Garnier, J.L. Béchade, et al., Tensile properties and deformation mechanisms of a 14Cr ODS ferritic steel, *J. Nucl. Mater.* 405 (2010) 95–100. doi:10.1016/j.jnucmat.2010.07.027.
- [60] F. Bergner, C. Pareige, M. Hernández-Mayoral, L. Malerba, C. Heintze, Application of a three-feature dispersed-barrier hardening model to neutron-irradiated Fe–Cr model alloys, *J. Nucl. Mater.* 448 (2014) 96–102.

doi:10.1016/j.jnucmat.2014.01.024.